Ultrasound GLCM texture analysis of radiation-induced parotid-gland injury in head-and-neck cancer radiotherapy: An *in vivo* study of late toxicity

Xiaofeng Yang

Department of Radiation Oncology, Emory University, Atlanta, Georgia 30322

Srini Tridandapani

Radiology and Imaging Sciences, Emory University School of Medicine, Atlanta, Georgia 30322

Jonathan J. Beitler and David S. Yu

Department of Radiation Oncology and Winship Cancer Institute, Emory University, Atlanta, Georgia 30322

Emi J. Yoshida

University of California Davis School of Medicine, Sacramento, California 95817

Walter J. Curran and Tian Liu[a)]

Department of Radiation Oncology and Winship Cancer Institute, Emory University, Atlanta, Georgia 30322

Abstract

Purpose: Xerostomia (dry mouth), secondary to irradiation of the parotid glands, is one of the most common side effects of head-and-neck cancer radiotherapy. Diagnostic tools able to accurately and efficiently measure parotid gland injury have yet to be introduced into the clinic.

This study's purpose is to investigate sonographic textural features as potential imaging signatures for quantitative assessment of parotid-gland injury after head-and-neck radiotherapy.

Methods: The authors have investigated a series of sonographic features obtained from the gray level co-occurrence matrix (GLCM) – a second order statistical method of texture analysis. These GLCM textural features were selected based on empirical observations that the normal parotid gland exhibits homogeneous echotexture, whereas the postradiotherapy parotid gland often exhibits heterogeneous echotexture. We employed eight sonographic features: (1) angular second moment (ASM), (2) inverse differential moment (IDM), (3) contrast, (4) variance, (5) correlation, (6) entropy, (7) cluster shade, and (8) cluster prominence. Altogether, sonographic properties of the parotid glands were quantified by their degrees of homogeneity (ASM and IDM), heterogeneity (contrast and variance), smoothness (correlation), randomness (entropy), and symmetry (cluster shade and prominence). The sonographic features were tested in a pilot study of 12 postradiotherapy patients and 7 healthy volunteers. The mean follow-up time for the postradiotherapy patients was 17.2 months (range: 12.1–23.9 months) and the mean radiation dose to the parotid glands was 32.3 Gy (range: 11.0–63.4 Gy). Each participant underwent one ultrasound study in which longitudinal (vertical) ultrasound scans were performed on the bilateral parotids – a total of 24 postirradiation and 14 normal parotid glands were examined. The 14 normal parotid glands served as the control group. A radiologist contoured the parotid glands on the B-mode images and the sonographic features were computed from the contoured region-of-interest.

Results: The authors observed significant differences ($p < 0.05$) in all sonographic features between the normal and postradiotherapy parotid glands. The sonographic findings were consistent with the clinical observations of the ultrasound images: normal parotid glands exhibited homogeneous texture, while the postradiotherapy parotid glands exhibited heterogeneous echotexture (e.g., hyperechoic lines and spots), which likely represents fibrosis.

Conclusions: The authors have demonstrated the feasibility of ultrasonic texture evaluation of parotid glands; and the sonographic features may serve as imaging signatures to assess radiation-induced parotid injury.

Keywords: xerostomia, radiation toxicity, sonographic features, GLCM texture, head-and-neck cancer

INTRODUCTION

Xerostomia (dry mouth) is a common side effect in patients treated with radiotherapy (RT) for their head-and-neck malignancies.[1] Patients with xerostomia frequently suffer from a wide range of conditions, such as pain, difficulty in speech and swallowing, increased rates of dental caries, and oral infection.[2] Furthermore, xerostomia is usually permanent, affecting many patients' quality of life (QOL) months and even years after their cancer treatment.[3]

Xerostomia has been under extensive clinical investigation over the past two decades.[4] As demonstrated by previous prospective studies, the most important predictors for xerostomia are the radiation dose and irradiated volume within the parotid glands.[2, 5, 6, 7, 8] Recent advances in conformal RT enable us to spare the parotid glands while delivering adequate radiation doses to the tumor targets, and have thus opened up a new avenue to prevent xerostomia.[1, 5] Nevertheless, the mechanism of salivary gland dysfunction is not yet fully understood. Diagnostic tools able to accurately and efficiently measure parotid gland injury have yet to be introduced into the clinic.

Early imaging studies have employed CT, MRI, and ultrasound; each imaging modality showed some degree of success. Volume reduction of parotid glands after RT has been observed in previous studies using computed tomography (CT) (Refs. [9] and [10]) and magnetic resonance imaging (MRI).[11, 12, 13, 14, 15, 16, 17] In the last ten years, researchers have been exploring ultrasound to evaluate the post-RT parotid gland.[18] In Doppler studies of late toxicity,[19, 20] significant differences were demonstrated in the high peak systolic velocity, resistive index, and pulsatility between post-irradiation and control parotid glands. With regard to gray scale image features, increased heterogeneity was reported in the post-RT parotid glands.[21] However, the echogenicity and echotexture of the parotid glands were evaluated through the examiner's interpretation of B-mode images. These subjective interpretations may not be able to capture clinically relevant yet subtle changes in echogenicity and echotexture.

In search of meaningful imaging signatures to assist in the diagnosis of radiation-induced parotid injury, we explored statistical analysis methods of the parotid-gland ultrasound images. In a previous paper, we demonstrated that first-order statistical features derived from the echo histogram could provide quantitative measures of postradiotherapy parotid injury.[22] In this report, we investigated second-order statistical texture features based on the gray level co-occurrence matrix (GLCM). Since the introduction of GLCM by Haralick in the 1970s,[23] GLCM has been widely used as texture measurements in medical imaging. Over the years, many researchers have used GLCM texture analysis of ultrasound images for cancer diagnoses in various organs, ranging from the liver[24] and breast[25, 26, 27, 28, 29, 30] to the parotid gland.[31] Our work is the first to investigate the GLCM textural features for the quantitative evaluation of radiation-induced parotid gland injury. The clinical feasibility was demonstrated in an *in vivo* pilot study of 12 post-RT patients and 7 healthy volunteers. These sonographic features may serve as imaging signatures to assess parotid injury, and provide useful information on changes in gland morphology and architectural integrity that facilitate further insight into the etiology of xerostomia.

GLCM METHOD

Defining GLCM

In this paper, we briefly summarize the computation of the GLCM and define the textural features employed. The GLCM texture method is a

way of extracting second order statistical texture features from gray-level images, such as ultrasound B-mode images. A GLCM is a matrix where the number of rows and columns is equal to the number of quantized gray levels, Ng, in the image. The matrix element $p(i, j)$ is the set of second order statistical probability values for changes between gray level i and j at a particular displacement distance (d) and angle (θ).

To illustrate this method, suppose an image to be analyzed has Nx columns and Ny rows. The gray level appearing at each pixel is quantized to Ng levels. Let $L_x = \{1, 2, …, N_x\}$ be the columns, $L_y = \{1, 2, …, N_y\}$ be the rows, and $G_x = \{0, 1, …, N_g − 1\}$ be the set of Ng quantized gray levels. The image can be represented as a function that assigns some gray level in G to each pixel or pair of coordinates in $L_y \times L_x$; $L_y \times L_x \rightarrow G$. The texture-context information is specified by the matrix of a relative frequency $C(i, j)$. $C(i, j)$ represents the number of occurrences of gray levels i and j within the window, at a certain (d, θ) pair. The probability measure can be defined as

$$Pro(x) = \{p(i, j)|(d, \theta)\},$$

(1)

where $p(i, j)$ is defined as

$$p\left(i, j\right) = \frac{C(i, j)}{\sum_{i=0}^{N_g-1} \sum_{j=0}^{N_g-1} C(i, j)}.$$

(2)

The sum in the denominator thus represents the total number of gray level pairs (i, j) within the window and is bounded by an upper limit of $N_g \times N_g$.

The means for the columns and rows of the matrix are, respectively, defined as

$$u_x = \sum_{i=0}^{N_g-1} \sum_{j=0}^{N_g-1} i \cdot p(i, j)$$

(3)

and

$$u_y = \sum_{i=0}^{N_g-1} \sum_{j=0}^{N_g-1} j \cdot p(i,j).$$

(4)

The standard deviations for the columns and rows of the matrix are, respectively, defined as

$$\sigma_x = \sum_{i=0}^{N_g-1} \sum_{j=0}^{N_g-1} (i - u_x)^2 \cdot p(i,j)$$

(5)

and

$$\sigma_y = \sum_{i=0}^{N_g-1} \sum_{j=0}^{N_g-1} (j - u_y)^2 \cdot p(i,j).$$

(6)

Researchers have investigated the various aspects of co-occurrence texture features.[32, 33] These investigations are performed to produce recommendations on how to set necessary parameters N_g, d, and θ. When choosing the quantized gray level (matrix dimension) N_g, a smaller N_g value accelerates the calculation of the co-occurrence texture features and reduces noise, however, this is offset by a reduction of information. In other words, coarser quantization would reduce both classification accuracy and feature space discernability of the classes. In our study, the ultrasound B-mode images were 8-bit gray level images (256 gray levels). Usually, 16 gray levels are sufficient for discrimination of textures for 8-bit gray level images.[34] Therefore, we used 16 for the gray level quantization (N_g) to balance the computation time and preservation of image information. We chose a displacement vector of $d = 4$ in our analyses.[30] The nominal ultrasound frequency utilized was 10 MHz; hence, the ultrasound wavelength is 0.15 mm and the axial resolution is ∼0.30 mm. For the B-mode image, the pixel size along the beam prop-

agation direction was 0.08 mm/pixel, therefore, a four-pixel distance (d = 4) represented one resolution cell. Depending upon the textures, the orientation could produce either similar or distinctively different GLCM. Here, we tested a set of four angles (θ) for d = 4: 0°, 45°, 90°, and 135°.

GLCM textural features

In this study, we investigated eight textural features to quantitatively evaluate the textural characteristics of the parotid glands on ultrasound images. These features were selected based on previous clinical observations by our group as well as others.[19, 21] For example, a previous study has reported homogeneous echotexture in normal parotid glands and heterogeneous echotexture in post-RT parotid glands.[19] The eight textural features are defined as follows.

Angular second moment (ASM, Energy)

$$\text{ASM} = \sum_{i=0}^{N_g-1} \sum_{j=0}^{N_g-1} p(i,j)^2 \tag{7}$$

ASM, also known as energy, is a measure of homogeneity of an image.[35] A homogeneous scene will contain only a few gray levels, so that GLCM will have a few but relatively high values of $p(i,j)$. Thus, the sum of squares will be high. It is the monotonic gray-level transition; higher values indicate textural uniformity. Therefore, when the image is homogeneous, the ASM will have high values.

Inverse difference moment (IDM)

$$\text{IDM} = \sum_{i=0}^{N_g-1} \sum_{j=0}^{N_g-1} \frac{1}{1+(i-j)^2} p(i,j) \tag{8}$$

IDM measures the local homogeneity of an image. The incidence of co-occurrence of pixel pairs is enhanced when they are close in gray-scale value and thus increases the IDM value. Because of the weighting factor $(1 + (i - j)^2)^{-1}$, it will get small contributions from inhomogeneous areas $i \neq j$. The result is a low IDM value for inhomogeneous images, and a relatively higher value for homogeneous images.

Contrast

$$\text{Con} = \sum_{k=0}^{N_g-1} k^2 \left\{ \sum_{i=0}^{N_g-1} \sum_{j=0}^{N_g-1} p(i,j) || i - j| = k \right\} \tag{9}$$

Contrast is a measure of the local variations presented in an image. This measure of contrast favors contributions from $p(i,j)$ away from the diagonal. It is highly correlated with the difference between the highest and the lowest values of a continuous set of pixels, particularly when the value of the displacement vector is 1.[36] If there is a large amount of variation in an image, the contrast will be high.

Variance

$$\begin{aligned} \text{Var} \;=\; & \sum_{i=0}^{N_g-1} \sum_{j=0}^{N_g-1} (i - u_x)^2 \cdot p(i,j) \\ & + \sum_{i=0}^{N_g-1} \sum_{j=0}^{N_g-1} (j - u_y)^2 \cdot p(i,j) \end{aligned} \tag{10}$$

Variance puts relatively high weights on the elements that differ from the average value of $p(i,j)$. It refers to the gray-level variability of the pixel pairs and is a measurement of heterogeneity. Variance increases when the gray-scale values differ from their means. Unlike contrast, variance has no spatial frequency. Although a high variance is suggestive of a high contrast value, the converse relationship does not apply.[37]

Correlation

$$\text{Cor} = \frac{\sum_{i=0}^{N_g-1} \sum_{j=0}^{N_g-1} (ij) \cdot p(i,j) - u_x u_y}{\sigma_x \sigma_y} \tag{11}$$

Correlation is a measure of the linear dependency of gray levels on those of neighboring pixels or specified points. It indicates local gray-level dependency on the texture image; higher values can be obtained for similar gray-level regions.

Entropy

$$\text{Ent} = -\sum_{i=0}^{N_g-1} \sum_{j=0}^{N_g-1} p(i,j) \log(p(i,j)) \tag{12}$$

Entropy measures the randomness of the image texture (intensity distribution). Entropy is the highest when all the probabilities $p(i,j)$ are equal, and smaller when the entries in $p(i,j)$ are unequal. Therefore, a homogeneous image will result in a lower entropy value, while an inhomogeneous (heterogeneous) region will result in a higher entropy value.

Cluster shade

$$\text{Sha} = \sum_{i=0}^{N_g-1} \sum_{j=0}^{N_g-1} (i+j-u_x-u_y)^3 p(i,j) \tag{13}$$

Cluster shade is a measure of the skewness of the matrix and is believed to gauge the perceptual concepts of uniformity.[38] A new "$i + j$" image

is created, having a range of integer intensities from 0 to $2(N_g - 1)$. The u_{i+j} value is computed and stored for the first neighborhood of the image, and is subsequently updated as the neighborhood is moved by one pixel. When the cluster shade is high, the image is asymmetric.

Cluster prominence

$$\text{Pro} = \sum_{i=0}^{N_g-1} \sum_{j=0}^{N_g-1} (i + j - u_x - u_y)^4 p(i, j) \tag{14}$$

Cluster prominence is also a measure of asymmetry.[38] When the cluster prominence value is high, the image is less symmetric. In addition, when cluster prominence value is low, there is a peak in the GLCM matrix around the mean values. For an ultrasound image, a low cluster prominence value indicates small variation in gray-scale.

PAROTID GLAND GLCM ANALYSIS PROCEDURE

Study participants

To test the GLCM imaging analysis concept, we conducted a pilot, *in vivo* clinical study. Between January and August 2011, we enrolled 19 participants (including 12 post-RT head-and-neck cancer patients and 7 healthy volunteers) under Emory University's Institutional Review Board approval. Each participant underwent one ultrasound study of their bilateral parotid glands; a total of 24 post-RT and 14 normal parotid glands were examined.

The post-RT patients (9 males and 3 females) ranged in age from 41 to 72 yr (mean: 54.9 ± 8.2 yr). All patients had previously received radiation treatment for their head-and-neck malignancies, such as laryngeal and oropharyngeal cancers. The mean radiation dose to the left parotid gland was 30.3 Gy (STD = 15.6 Gy, range: 11.0–63.4 Gy) and to the right parotid gland was 34.4 Gy (STD = 10.7 Gy, range: 21.5–51.4 Gy). Overall, the mean radiation dose to all parotid glands was 32.3 Gy (range: 11.0–63.4 Gy). The cross-sectional study is based on late toxicity, and all patients were scanned between 1 and 2 yr post-RT. The mean time between the completion of RT and the ultrasound scan was 17.2 months (STD = 4.3 months, range 12.1–23.9 months).

Serving as the control group for the study, the healthy subjects (5 males and 2 females) ranged in age from 27 to 60 yr (mean: 47.0 ± 10.0 yr). The exclusion criteria for the control group included subjects with clinical history of salivary gland diseases or head-and-neck cancers.

Ultrasound scans of the parotid glands

We established a standardized protocol for ultrasound scanning to facilitate accurate, quantitative measurements of the parotid glands. All ultrasound studies were performed using a clinical scanner (SonixTouch, Ultrasonix, British Columbia, Canada) with a linear array transducer (L14-5/38 probe, 128 elements). All ultrasound data were acquired with the same settings: 10 MHz center frequency, 1.00 cm focal length, 3 cm depth, 72% gain, 31 frames/s, and 80-dB dynamic range. This setting was determined by the radiologist (S.T.) and the medical physicist (T.L.) based on clinical experiences in parotid-gland examinations.

All participants were scanned in the upright seated position, and longitudinal (vertical) ultrasound scans were performed on the bilateral parotids (Fig. 1). During the ultrasound scan, a thin layer of ultrasound gel was used to ensure good coupling between the face and the ultrasound probe. The probe was placed perpendicular to the scan surface with minimal pressure applied to the face. All B-mode images were saved in 8-bit gray scale, and the intensity ranged from 0 to 255. Each B-mode image contained 488 (width) × 356 (depth) pixels with each pixel measuring 0.078×0.084 mm^2 in size.
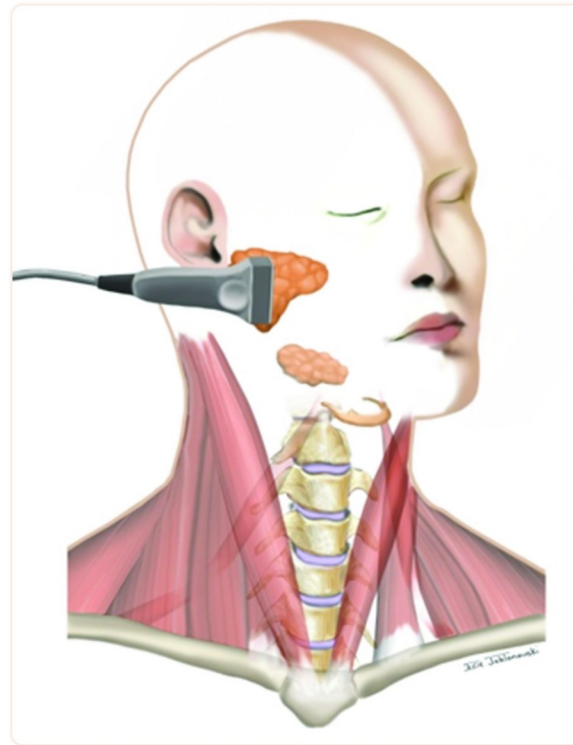
Figure 1

Illustration demonstrating ultrasound scanning of the parotid gland (drawn by Eric Jablonowski, Department of Radiology and Imaging Science, Emory University, Atlanta, GA).

Ultrasound image texture analysis with GLCM

We developed in-house signal processing software written in MATLAB® (Mathworks, Natick, MA) that displayed ultrasound images and computed GLCM sonographic features to assess radiation damage to the parotid glands. Prior to the data analysis, the boundaries of the parotid glands on the B-mode images were contoured by a radiologist (S.T.). As described in Sec. 2, eight sonographic texture parameters were computed from GLCM: variance, correlation, IDM, ASM, contrast, entropy, cluster shade, and cluster prominence.

The sonographic parameters derived from the echo histograms were expressed as means and standard deviations. An unpaired t-test was used to examine the significance of the difference between post-RT and normal parotid-gland measurements. A value of $p < 0.05$ was considered to be statistical significance.

RESULTS

Figure 2 shows two example cases in our study—a normal and a post-RT parotid gland. On the left are the ultrasound image and corresponding GLCM of a normal parotid gland obtained from a 41 yr-old healthy volunteer. The region of the normal parotid gland on the ultrasound image showed homogeneous echotexture and fine soft tissue echogenicity. The corresponding GLCMs were similar at 0°, 45°, 90°, and 135°, with the exception that it is slightly narrower at 0°. On the right are the ultrasound image and corresponding GLCM maps of a left parotid gland obtained from a 52 yr-old patient, 22 months post-RT for his laryngeal cancer. He received 70.29 Gy to the primary tumor and his left parotid gland received 41.5 Gy. From the patient's self-assessment, he experienced moderate xerostomia at the time of the ultrasound study. The region of the post-RT parotid gland on the ultrasound image showed heterogeneity in echotexture and coarse soft tissue echogenicity. Again, the corresponding GLCMs were similar at 0°, 45°, 90°, and 135°, with the exception that the GLCM is slightly narrower at 0°. A similar computation was performed for all participants, i.e., on all 24 post-RT and 14 normal parotid glands.
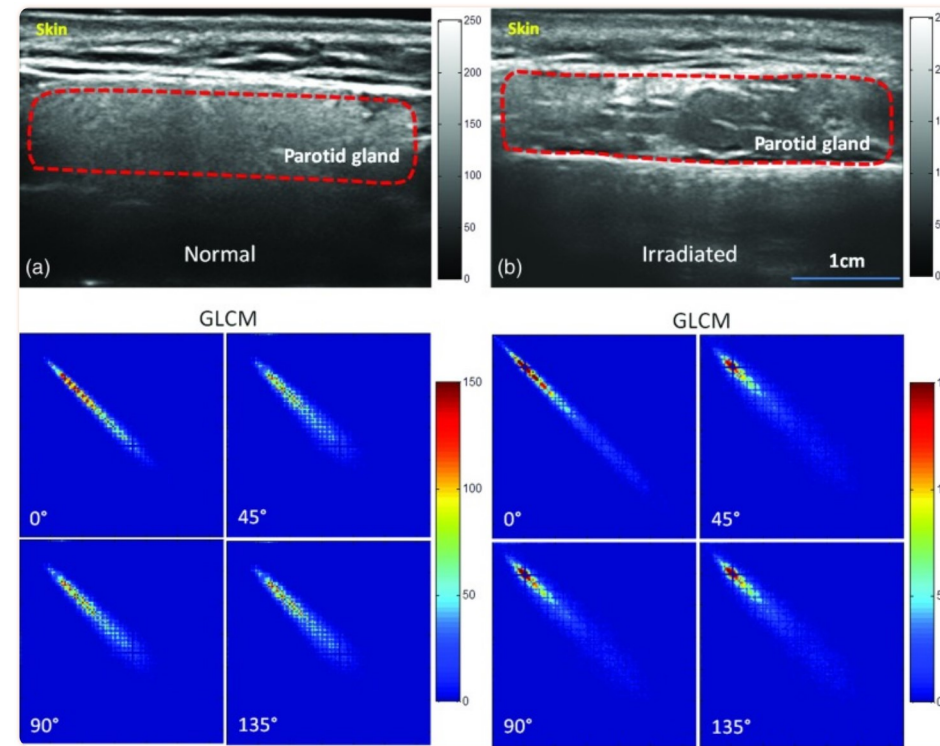
Figure 2

Ultrasound B-mode images of normal (a) and post-RT (b) parotid glands and their GLCM in four directions (0°, 45°, 90°, and 135°). (a) Ultrasound image of the left parotid gland of a 41-yr-old healthy volunteer, revealing homogeneous echotexture and fine soft tissue echogenicity. (b) Ultrasound images of the left parotid gland of a 52-yr-old laryngeal cancer patient, 22 months post-RT, revealing heterogeneous echotexture.

As shown in Table 1, strong differences between the control (n = 14) and post-RT (n = 24) groups are demonstrated in all eight GLCM sonographic features. Compared with the features of the normal parotid glands, the ASM, IDM, and correlation values decreased for the irradiated glands, whereas all other features including contrast, variance, cluster shade, and prominence increased. The percentage changes of the post-RT group to the normal group for all GLCM parameters were also calculated to show the relative changes post radiation.

Table 1

Comparison of sonographic texture features (Mean ± STD) between the normal (n = 14) and post-RT (n = 24) groups.

Feature	Subjects	ASM (×10⁴)	IDM (×10²)	Con (×10⁻²)	Var (×10⁻²)	Cor (×10⁴)	Ent	Shade (×10⁻⁴)	Pro (×10⁻⁶)
0°	Normal group	6.4 ± 1.6	9.0 ± 1.0	2.1 ± 0.5	2.9 ± 1.0	23.1 ± 4.8	7.6 ± 0.3	2.17 ± 2.09	5.3 ± 4.6
	Post-RT group	3.6 ± 1.0	9.0 ± 1.9	3.3 ± 1.1	9.7 ± 3.5	8.9 ± 2.8	8.3 ± 0.2	23.3 ± 17.7	59.1 ± 47.1
	Percent change (%)	−44.0	−0.5	58.1	233.3	−61.4	9.3	969.9	1011.4
	p-value	<0.001	0.920	<0.001	<0.001	<0.001	<0.001	<0.001	<0.001
45°	Normal group	5.9 ± 1.8	7.4 ± 1.3	3.9 ± 1.4	2.8 ± 1.0	10.5 ± 6.1	7.7 ± 0.4	0.8 ± 0.1	2.3 ± 1.9
	Post-RT group	2.8 ± 0.8	6.2 ± 1.5	10.2 ± 4.5	9.1 ± 3.6	5.3 ± 2.1	8.5 ± 0.2	12.3 ± 10.7	29.7 ± 24.6
	Percent change (%)	−52.5	−15.9	160.5	224.3	−49.1	11.2	1358.3	1182.7
	p-value	<0.001	0.149	<0.001	<0.001	0.001	<0.001	<0.001	<0.001
90°	Normal group	6.0 ± 1.8	7.7 ± 1.2	3.8 ± 1.3	2.8 ± 1.0	10.7 ± 6.0	7.7 ± 0.4	0.9 ± 0.1	2.4 ± 1.9
	Post-RT group	2.9 ± 0.9	6.4 ± 1.5	10.0 ± 4.2	9.2 ± 3.6	5.5 ± 2.1	8.5 ± 0.2	12.6 ± 11.5	30.9 ± 27.1
	Percent change (%)	−52.0	−17.4	161.8	223.8	−48.9	11.1	1331.8	1181.3
	p-value	<0.001	0.004	<0.001	<0.001	0.001	<0.001	<0.001	<0.001
135°	Normal group	5.9 ± 1.8	7.4 ± 1.2	3.9 ± 1.3	2.8 ± 1.0	9.8 ± 3.3	7.7 ± 0.4	0.9 ± 0.1	2.4 ± 2.0
	Post-RT group	2.8 ± 0.8	6.2 ± 1.4	10.4 ± 4.3	9.2 ± 3.6	5.2 ± 2.2	8.5 ± 0.2	12.3 ± 11.5	30.1 ± 27.1
	Percent change (%)	−52.8	−16.4	169.3	225.6	−47.0	11.2	1256.3	1163.8
	p-value	<0.001	0.010	<0.001	<0.001	<0.001	<0.001	<0.001	<0.001
Average	Normal group	6.1 ± 1.7	7.9 ± 1.3	3.4 ± 1.4	2.8 ± 1.0	13.5 ± 7.5	7.7 ± 0.3	1.2 ± 1.5	3.1 ± 3.0
	Post-RT group	3.0 ± 0.8	6.9 ± 1.4	8.5 ± 4.3	9.3 ± 3.6	6.2 ± 2.2	8.5 ± 0.2	15.1 ± 11.5	37.4 ± 27.1
	Percent change (%)	−50.2	−12.0	147.8	226.8	−53.9	10.7	1158.5	1105.5

[1]Note: Percent change (%) = (post-RT parameter value – normal parameter value) *100/normal parameter value.

With the exception of IDM values at angles 0° and 45°, significant differences between the normal and post-RT parotid glands are noted in all the examined angles ($p < 0.05$). Similar results were obtained for each feature at various angles. Ninety degrees (beam direction) appeared to be the angle at which the greatest post-RT changes were illustrated. Figure 3 shows the average textural features of the control and post-RT groups at 90°.
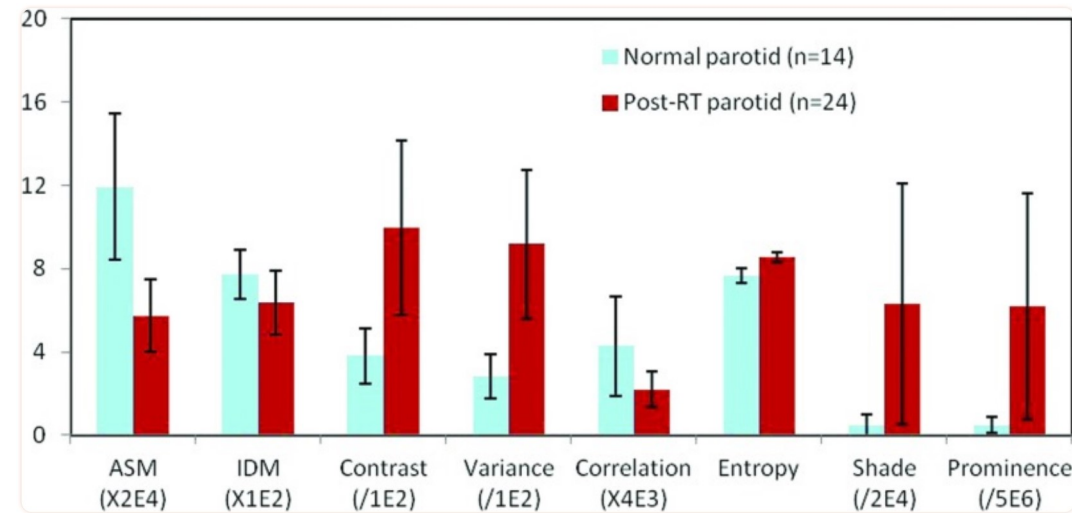

Figure 3

Textural features (Mean ± STD) of the normal and post-RT parotid glands ($N_g = 16$, $d = 4$, $\theta = 90°$).

DISCUSSION

Radiation therapy is a prevalent treatment modality for head-and-neck cancers. In the United States, thousands of patients receive RT for their head-and-neck cancers each year.[5, 6] Radiation-related xerostomia impairs the physiologic and psychological well-being of many patients. Although previous studies have demonstrated that the severity of salivary gland damage increases with radiation dose and exposed gland volume,[7, 8] the mechanism of radiation damage is poorly understood.

In this clinical study, we demonstrated the feasibility of utilizing GLCM textural features to assess radiation-induced parotid injury. Our findings from GLCM features are consistent with previous ultrasound studies that have similarly reported changes in echogenicity and echotexture of post-RT parotid glands.[19, 20] Our sonographic texture analysis method was motivated by empirical clinical observations that the sonographic appearance of post-RT parotid glands was markedly different than normal parotid glands. Parotid glands in the healthy subjects tended to be more homogenous, whereas parotid glands in the treated patients were predominantly heterogeneous. In addition, hypoechoic areas and hyperechoic lines or spots were found in post-RT parotid glands (see Fig. 2). Our GLCM method offers an attractive alternative to the subjective interpretation of the conventional sonography, i.e., B-mode evaluation, currently employed in the clinic. Specifically, our GLCM features provide detailed quantification of textural changes, which improves upon the subjective nature of current radiologic interpretations of ultrasound images.

We observed significant differences in eight textural features between the normal and post-RT parotid glands. Texture features ASM and IDM are associated with overall and local homogeneity. Both features decreased in the post-RT parotid glands, suggesting an increased level of heterogeneity. Contrast and variance are features that are related to local and global variability. Higher contrast and variance values were observed in post-RT parotid glands. These results suggest that post-RT parotid glands possess complex texture and larger variations, whereas normal parotid glands seem more uniform. Correlation is a measure of gray level linear dependence between neighboring pixels and entropy is a measure of the texture randomness. The post-RT parotid glands had decreased correlation and increased entropy. Cluster shade and cluster prominence are measures of the skewness or asymmetry. Post-RT parotid glands showed increased cluster shade and prominence, indicating a lack of symmetry. Among the eight textual features, ASM, contrast, and variance seemed to be most promising due to their relative large separation, small standard deviation, and significance in differentiating the two groups (Fig. 3).

Furthermore, our findings are consistent with histopathological findings of the post-RT parotid glands. Histological studies have reported that normal parotid glands are filled with homogenous serous acinar cells that contain densely packed translucent secretory granules.[39, 40] Those densely packed cells and granules provide uniform and highly reflective interfaces for the ultrasound beam,[41] producing for the homogeneous and hyperechoic appearance of the normal parotid glands. After irradiation, many acini are lost with the remaining acini appearing larger than normal and more disorganized.[42] The heterogeneous echo-pattern of post-RT parotid gland is likely due to the presence of nonuniform ultrasound reflective interfaces from the disorganized acinar cell arrangement after parenchymal loss and acinar atrophy.[40] Radiation-induced fibrosis and chronic sialadenitis with inflammatory infiltrate are also found in the post-RT parotid glands.[43, 44, 45, 46] The heterogeneous echo texture of post-RT parotid glands may be due to the presence of inflammatory infiltrate patches, which appears as multiple hypoechoic areas, as well as the presence of fibrosis, which appears as hyperechoic lines or spots.

This pilot study has four primary limitations. First, the sample size of 19 participants is small. Nevertheless, the feasibility of using ultrasound GLCM textural features to evaluate post-RT parotid injury is demonstrated. Second, the dose delivered to each parotid gland is an important

factor that is not fully evaluated in the study. Third, we compared textural features between normal and post-RT parotid glands without comparing clinical end points, such as patient assessment of dry month, due to the small sample size. Further studies that correlate the sonographic features of parotid glands with radiation dose received and with the clinical evaluation of xerostomia are warranted. Fourth, in this study, all parotid glands were manually contoured by the radiologist. Automatic segmentation of the parotid glands could eliminate the physician's subjective interpretations and interobserver variability. We are conducting a longitudinal study with a larger cohort to address these limitations.

In summary, we demonstrated the feasibility of using sonographic texture features as imaging signatures to assess parotid gland injury in patients post head-and-neck RT. Our quantitative ultrasound method offers a potential imaging tool to assess parotid injury. Such a tool may become increasing valuable as we increase the therapeutic ratio for successful treatment of head-and-neck cancer while minimizing normal-tissue toxicity.

CONCLUSIONS

We have investigated a family of objective sonographic features derived from GLCM in order to provide a noninvasive, objective, and reliable means of measuring radiation-induced parotid-gland injury. Currently, radiation toxicity is exclusively evaluated by clinical history and physical examination making it susceptible to interobserver variability. Indeed, ultrasound could be a attractive alternative to the current gold standard of clinical assessment, since it is noninvasive and safe. Compared with CT or MRI, ultrasound is cost-effective, thus offering the potential for wide clinical application. The sonographic texture features could provide quantification of the echogenicity and echotexture of parotid glands. Objective, noninvasive imaging assessments of radiation toxicity, particularly those assessments that can be identified as measures of treatment outcome and quality of life, could provide a valuable tool to post-RT patient care.

ACKNOWLEDGMENTS

References

1. Chao K. S. C., Deasy J. O., Markman J., Haynie J., Perez C. A., Purdy J. A., and Low D. A., "A prospective study of salivary function sparing in patients with head-and-neck cancers receiving intensity-modulated or three-dimensional radiation therapy: Initial results," *Int. J. Radiat. Oncol. Biol. Phys.* 49, 907–916 (2001). 10.1016/S0360-3016(00)01441-3

[PubMed] [CrossRef] [Google Scholar]

2. Eisbruch A., Rhodus N., Rosenthal D., Murphy B., Rasch C., Sonis S., Scarantino C., and Brizel D., "How should we measure and report radiotherapy-induced xerostomia?," *Semin. Radiat. Oncol.* 13, 226–234 (2003). 10.1016/S1053-4296(03)00033-X [PubMed] [CrossRef] [Google Scholar]

3. Lin A., Kim H. M., Terrell J. E., Dawson L. A., Ship J. A., and Eisbruch A., "Quality of life after parotid-sparing IMRT for head-and-neck cancer: A prospective longitudinal study," *Int. J. Radiat. Oncol. Biol. Phys.* 57, 61–70 (2003). 10.1016/S0360-3016(03)00361-4 [PubMed] [CrossRef] [Google Scholar]

4. Cooper J. S., Fu K., Marks J., and Silverman S., "Late effects of radiation-therapy in the head and neck region," *Int. J. Radiat. Oncol. Biol. Phys.* 31, 1141–1164 (1995). 10.1016/0360-3016(94)00421-G [PubMed] [CrossRef] [Google Scholar]

5. Eisbruch A., "Clinical aspects of IMRT for head-and-neck cancer," *Med. Dosim.* 27, 99–104 (2002). 10.1016/S0958-3947(02)00091-2 [PubMed] [CrossRef] [Google Scholar]

6. Eisbruch A., Kim H. M., Terrell J. E., Marsh L. H., Dawson L. A., and Ship J. A., "Xerostomia and its predictors following parotid-sparing irradiation of head-and-neck cancer," *Int. J. Radiat. Oncol. Biol. Phys.* 50, 695–704 (2001). 10.1016/S0360-3016(01)01512-7 [PubMed] [CrossRef] [Google Scholar]

7. Eisbruch A., Ten Haken R. K., Kim H. M., Marsh L. H., and Ship J. A., "Dose, volume, and function relationships in parotid salivary glands following conformal and intensity-modulated irradiation of head and neck cancer," *Int. J. Radiat. Oncol. Biol. Phys.* 45, 577–587 (1999). 10.1016/S0360-3016(99)00247-3 [PubMed] [CrossRef] [Google Scholar]

8. Deasy J. O., Moiseenko V., Marks L., Chao K. S. C., Nam J., and Eisbruch A., "Radiotherapy dose-volume effects on salivary gland function," *Int. J. Radiat. Oncol. Biol. Phys.* 76, S58–S63 (2010). 10.1016/j.ijrobp.2009.06.090 [PMC free article] [PubMed] [CrossRef] [Google Scholar]

9. Barker J. L., Garden A. S., Ang K. K., O'Daniel J. C., Wang H., Court L. E., Morrison W. H., Rosenthal D. I., Chao K. S. C., Tucker S. L., Mohan R., and Dong L., "Quantification of volumetric and geometric changes occurring during fractionated radiotherapy for head-and-neck cancer using an integrated CT/linear accelerator system," *Int. J. Radiat. Oncol. Biol. Phys.* 59, 960–970 (2004). 10.1016/j.ijrobp.2003.12.024 [PubMed] [CrossRef] [Google Scholar]

10. Lee C., Langen K. M., Lu W., Haimerl J., Schnarr E., Ruchala K. J., Olivera G. H., Meeks S. L., Kupelian P. A., Shellenberger T. D., and Mañon R. R., "Evaluation of geometric changes of parotid glands during head and neck cancer radiotherapy using daily MVCT and automatic deformable registration," *Radiother. Oncol.* 89, 81–88 (2008). 10.1016/j.radonc.2008.07.006 [PubMed] [CrossRef] [Google Scholar]

11. Nömayr A., Lell M., Sweeney R., Bautz W., and Lukas P., "MRI appearance of radiation-induced changes of normal cervical tissues," *Eur. Radiol.* 11, 1807–1817 (2001). 10.1007/s003300000728 [PubMed] [CrossRef] [Google Scholar]

12. Wada A., Uchida N., Yokokawa M., Yoshizako T., and Kitagaki H., "Radiation-induced xerostomia: Objective evaluation of salivary gland injury using MR sialography," *Am. J. Neuroradiol.* 30, 53–58 (2009). 10.3174/ajnr.A1347 [PMC free article] [PubMed] [CrossRef] [Google Scholar]

13. Lee F. K. H., King A. D., Kam M. K. M., Ma B. B. Y., and Yeung D. K. W., "Radiation injury of the parotid glands during treatment for head and neck cancer: Assessment using dynamic contrast-enhanced MR imaging," *Radiat. Res.* 175, 291–296 (2011). 10.1667/RR2370.1 [PubMed] [CrossRef] [Google Scholar]

14. Yoshino N., Yamada I., Ohbayashi N., Honda E., Ida M., Kurabayashi T., Maruyama K., and Sasaki T., "Salivary glands and lesions: Evaluation of apparent diffusion coefficients with split-echo diffusion-weighted MR imaging–Initial results," *Radiology* 221, 837–842 (2001). 10.1148/radiol.2213010131 [PubMed] [CrossRef] [Google Scholar]

15. Shah G. V., "MR imaging of salivary glands," *Magn. Reson. Imaging Clin. N. Am.* 10, 631–662 (2002). 10.1016/S1064-9689(02)00015-6 [PubMed] [CrossRef] [Google Scholar]

16. Sumi M., Takagi Y., Uetani M., Morikawa M., Hayashi K., Kabasawa H., Aikawa K., and Nakamura T., "Diffusion-weighted echoplanar MR imaging of the salivary glands," *AJR, Am. J. Roentgenol.* 178, 959–965 (2002). [PubMed] [Google Scholar]

17. Shah G. V., "MR imaging of salivary glands," *Neuroimaging Clin. N. Am.* 14, 777–808 (2004). 10.1016/j.nic.2004.07.010 [PubMed] [CrossRef] [Google Scholar]

18. Bhatia K. S. S., Rasalkar D. D., Lee Y. P., Wong K. T., King A. D., Yuen H. Y., and Ahuja A. T., "Evaluation of real-time qualitative sonoelastography of focal lesions in the parotid and submandibular glands: Applications and limitations," *Eur. Radiol.* 20, 1958–1964 (2010). 10.1007/s00330-010-1756-0 [PubMed] [CrossRef] [Google Scholar]

19. Ying M., Wu V. W. C., and Kwong D. L. W., "Comparison of sonographic appearance of normal and postradiotherapy parotid glands: A preliminary study," *Ultrasound Med. Biol.* 33, 1244–1250 (2007). 10.1016/j.ultrasmedbio.2007.02.016 [PubMed] [CrossRef] [Google Scholar]

20. Cheng S. C., Ying M. T., Kwong D. L., and Wu V. W., "Sonographic appearance of parotid glands in patients treated with intensity-modulated radiotherapy or conventional radiotherapy for nasopharyngeal carcinoma," *Ultrasound Med. Biol.* 37, 220–230 (2011). 10.1016/j.ultrasmedbio.2010.11.002 [PubMed] [CrossRef] [Google Scholar]

21. Cheng S. C. H., Wu V. W. C., Kwong D. L. W., and Ying M. T. C., "Assessment of post-radiotherapy salivary glands," *Br. J. Radiol.* 84, 393–402 (2011). 10.1259/bjr/66754762 [PMC free article] [PubMed] [CrossRef] [Google Scholar]

22. Yang X., Tridandapani S., Beitler J. J., Yu D. S., Yoshida E. J., Curran W. J., and Liu T., "Ultrasound histogram assessment of parotid gland injury following head-and-neck radiotherapy: A feasibility study," *Ultrasound Med. Biol.* 38, 1514–1521 (2012). 10.1016/j.ultrasmedbio.2012.05.005 [PMC free article] [PubMed] [CrossRef] [Google Scholar]

23. Haralick R. M., Shanmugam K., and Dinstein I., "Textural features for image classification," *IEEE Trans. Syst. Man Cybern.* Smc3, 610–621 (1973). 10.1109/TSMC.1973.4309314 [CrossRef] [Google Scholar]

24. Layer G., Zuna I., Lorenz A., Zerban H., Haberkorn U., Bannasch P., van Kaick G., and Räth U., "Computerized ultrasound B-scan texture analysis of experimental fatty liver-disease: Influence of total lipid content and fat deposit distribution," *Ultrason. Imaging* 12, 171–188 (1990). 10.1016/0161-7346(90)90009-M [PubMed] [CrossRef] [Google Scholar]

25. Sivaramakrishna R., Powell K. A., Lieber M. L., Chilcote W. A., and Shekhar R., "Texture analysis of lesions in breast ultrasound images," *Comput. Med. Imaging Graph.* 26, 303–307 (2002). 10.1016/S0895-6111(02)00027-7 [PubMed] [CrossRef] [Google Scholar]

26. Kuo W. J., Chang R. F., Lee C. C., Moon W. K., and Chen D. R., "Retrieval technique for the diagnosis of solid breast tumors on sonogram," *Ultrasound Med. Biol.* 28, 903–909 (2002). 10.1016/S0301-5629(02)00541-0 [PubMed] [CrossRef] [Google Scholar]

27. Chang R. F., Wu W. J., Moon W. K., and Chen D. R., "Improvement in breast tumor discrimination by support vector machines and speckle-emphasis texture analysis," *Ultrasound*

Med. Biol. 29, 679–686 (2003). 10.1016/S0301-5629(02)00788-3 [PubMed] [CrossRef] [Google Scholar]

28. Chen D. R., Chang R. F., and Huang Y. L., "Breast cancer diagnosis using self-organizing map for sonography," *Ultrasound Med. Biol.* 26, 405–411 (2000). 10.1016/S0301-5629(99)00156-8 [PubMed] [CrossRef] [Google Scholar]

29. Liao Y. Y., Tsui P. H., Li C. H., Chang K. J., Kuo W. H., Chang C. C., and Yeh C. K., "Classification of scattering media within benign and malignant breast tumors based on ultrasound texture-feature-based and Nakagami-parameter images," *Med. Phys.* 38, 2198–2207 (2011). 10.1118/1.3566064 [PubMed] [CrossRef] [Google Scholar]

30. Alvarenga A. V., Pereira W. C. A., Infantosi A. F. C., and Azevedo C. M., "Complexity curve and grey level co-occurrence matrix in the texture evaluation of breast tumor on ultrasound images," *Med. Phys.* 34, 379–387 (2007). 10.1118/1.2401039 [PubMed] [CrossRef] [Google Scholar]

31. Mailloux G. E., Bertrand M., Stampfler R., and Ethier S., "Texture analysis of ultrasound B-mode images by segmentation," *Ultrason. Imaging* 6, 262–277 (1984). 10.1016/0161-7346(84)90012-9 [PubMed] [CrossRef] [Google Scholar]

32. Clausi D. A. and Zhao Y., "Rapid extraction of image texture by co-occurrence using a hybrid data structure," *Comput. Geosci.* 28, 763–774 (2002). 10.1016/S0098-3004(01)00108-X [CrossRef] [Google Scholar]

33. Clausi D. A., "An analysis of co-occurrence texture statistics as a function of grey level quantization," *Can. J. Remote Sens.* 28, 45–62 (2002). 10.5589/m02-004 [CrossRef] [Google Scholar]

34. Xu D. H., Kurani A. S., Furst J. D., and Raicu D. S., "Run-length encoding for volumetric texture," *Proceedings of the Fourth IASTED International Conference on Visualization, Imaging, and Image Processing* (Marbella, Spain, 2004), 534–539.

35. Gong P., Marceau D. J., and Howarth P. J., "A comparison of spatial feature-extraction algorithms for land-use classification with spot Hrv data," *Remote Sens. Environ.* 40, 137–151 (1992). 10.1016/0034-4257(92)90011-8 [CrossRef] [Google Scholar]

36. Liu X. H., Clarke K., and Herold M., "Population density and image texture: A comparison study," *Photogramm. Eng. Remote Sens.* 72, 187–196 (2006). [Google Scholar]

37. Baraldi A. and Parmiggiani F., "An investigation of the textural characteristics associated with gray level cooccurrence matrix statistical parameters," *IEEE Trans. GISci. Remote Sens* 33, 293–304 (1995). 10.1109/36.377929 [CrossRef] [Google Scholar]

38. Unser M., "Sum and difference histograms for texture classification," *IEEE Trans. Pattern Anal. Mach. Intell.* 8, 118–125 (1986). 10.1109/TPAMI.1986.4767760 [PubMed] [CrossRef] [Google Scholar]

39. Henriksson R., Fröjd Ö., Gustafsson H., Johansson S., Yi-Qing C., Franzén L., and Bjermer L., "Increase in mast cells and hyaluronic acid correlates to radiation-induced damage and loss of serous acinar cells in salivary glands: The parotid and submandibular glands differ in radiation sensitivity," *Br. J. Cancer* 69, 320–326 (1994). 10.1038/bjc.1994.58 [PMC free article] [PubMed] [CrossRef] [Google Scholar]

40. Grehn A. L., Gustafsson H., Franzén L., Thornell L. E., and Henriksson R., "Ultrastructural morphometry of parotid acinar cells following fractionated irradiation," *Oral Oncol.* 33,

23–28 (1997). 10.1016/S0964-1955(96)00040-1 [PubMed] [CrossRef] [Google Scholar]

41. Katz P., Hartl D. M., and Guerre A., "Clinical ultrasound of the salivary glands," *Otolaryngol. Clin. North Am.* 42, 973–1000 (2009). 10.1016/j.otc.2009.08.009 [PubMed] [CrossRef] [Google Scholar]

42. Nagler R. M., "The enigmatic mechanism of irradiation-induced damage to the major salivary glands," *Oral Dis.* 8, 141–146 (2002). 10.1034/j.1601-0825.2002.02838.x [PubMed] [CrossRef] [Google Scholar]

43. Seifert G., "Etiology and differential diagnosis of sialadenitis," *Laryngorhinootologie* 74, 274–281 (1995). 10.1055/s-2007-997739 [PubMed] [CrossRef] [Google Scholar]

44. Radfar L. and Sirois D. A., "Structural and functional injury in minipig salivary glands following fractionated exposure to 70 Gy of ionizing radiation: An animal model for human radiation-induced salivary gland injury," *Oral Surg., Oral Med., Oral Pathol.* 96, 267–274 (2003). 10.1016/S1079-2104(03)00369-X [PubMed] [CrossRef] [Google Scholar]

45. Teymoortash A., Simolka N., Schrader C., Tiemann M., and Werner J. A., "Lymphocyte subsets in irradiation-induced sialadenitis of the submandibular gland," *Histopathology* 47, 493–500 (2005). 10.1111/j.1365-2559.2005.02256.x [PubMed] [CrossRef] [Google Scholar]

46. Konings A. W. T., Faber H., Cotteleer F., Vissink A., and Coppes R. P., "Secondary radiation damage as the main cause for unexpected volume effects: A histopathologic study of the parotid gland," *Int. J. Radiat. Oncol. Biol. Phys.* 64, 98–105 (2006). 10.1016/j.ijrobp.2005.06.042 [PubMed] [CrossRef] [Google Scholar]